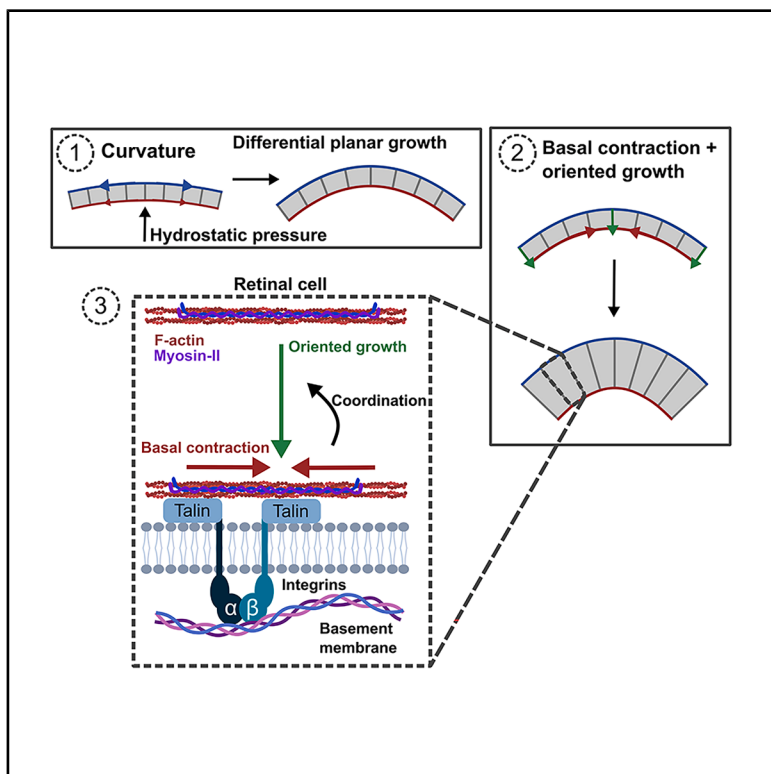


Integrins coordinate basal surface contraction and oriented cell growth to enable thickening of a curved epithelium

Graphical abstract



Authors

Courtney Lancaster, Angelika Manhart,
Franck Pichaud

Correspondence

angelika.manhart@univie.ac.at (A.M.),
f.pichaud@ucl.ac.uk (F.P.)

In brief

Lancaster et al. show uniform thickening of a curved epithelium, such as the developing *Drosophila* retina, is achieved through the coordination of oriented cell growth, which promotes cell elongation, and basal surface contraction. They find integrin adhesion and myosin-II are essential for this coordination.

Highlights

- Retinal curvature is induced as the tissue apical and basal surfaces expand
- Hydrostatic pressure plays an essential role in retinal curvature
- Retinal thickening requires coordinated cell elongation and basal contraction
- Basal regulation involving integrins and MyoII is required for retinal thickening

Article

Integrins coordinate basal surface contraction and oriented cell growth to enable thickening of a curved epithelium

Courtney Lancaster,¹ Angelika Manhart,^{3,4,*} and Franck Pichaud^{1,2,5,*}

¹Cell Biology of Tissue Architecture and Physiology Group, Laboratory for Molecular Cell Biology, University College London, London WC1E 6BT, UK

²Institute for the Physics of Living Systems, University College London, London WC1E 6BT, UK

³Faculty of Mathematics, University of Vienna, Vienna 1090, Austria

⁴Department of Mathematics, University College London, London WC1E 6BT, UK

⁵Lead contact

*Correspondence: angelika.manhart@univie.ac.at (A.M.), f.pichaud@ucl.ac.uk (F.P.)

<https://doi.org/10.1016/j.cub.2025.05.048>

SUMMARY

During development, tissues undergo morphogenesis to achieve their final form. This process relies on co-ordinated cell shape changes, which have predominantly been studied in one plane, at the apical (top) surface of developing tissues. However, tissues are three dimensional, often exhibiting deformations along multiple axes. To understand how morphogenesis is coordinated across tissue axes, we used the genetically amenable *Drosophila* retina, a curved, dome-shaped epithelium, as a model system. Using intravital imaging, we found that retinal curvature is induced early in development. Modeling early retinal development with a vertex model suggests that this curvature arises from differential planar growth between the apical and basal tissue surfaces. In addition, mechanical perturbation experiments revealed that inside-out fluid pressure plays a crucial role in promoting this curvature. Further combining computational modeling, genetic perturbations, and force-inference experiments, we demonstrate that uniform thickening of the curved retinal epithelium requires coordination of two key processes: growth, promoting cell elongation along the apical-basal axis of the tissue, and basal surface contraction. Remarkably, inhibiting basal surface contraction—both *in silico* and through genetic manipulations targeting the basal surface receptor integrin and non-muscle myosin-II—prevented cell elongation. We conclude that thickening of a curved epithelium, like the *Drosophila* retina, requires both integrin and non-muscle myosin-II to coordinate basal surface contraction and cell growth along the apical-basal axis of the tissue.

INTRODUCTION

Epithelia are found in most organs, where they form barriers between physiological compartments. In these tissues, cells coordinate their apical-basal (top-bottom) polarity to generate distinct tissue surfaces, which have different properties and functions. During development, remodeling of the apical and/or basal surfaces of epithelial cells promotes both in- and out-of-plane deformations to sculpt tissues in 3D.^{1–4} Apical cell geometry remodeling and cell movements have been well-studied in *Drosophila* tissues, where apical-lateral adherens junctions mechanically couple neighboring cells.^{5–7} In the gastrulating fly embryo,^{8–11} developing notum,¹² and eye epithelium,^{13–16} for example, apical geometry remodeling and the relative movement of cells in the plane of the tissue are coordinated through adherens junction remodeling. In all cases, adherens junction remodeling depends on the balance between intercellular adhesion and cortical tension.^{17–19} Macroscopic tissue deformations are induced as cells coordinate remodeling of their shape. This is the case, for example, when cells coordinate their apical

constriction to induce tissue invagination in the gastrulating fly embryo or during fold formation in epithelial development.^{20–23}

In the gastrulating fly embryo, cell apical constriction is induced by an apical-medial meshwork of non-muscle myosin-II (MyoII), which pulls radially onto the adherens junctions to reduce the apical area of cells.²¹ Similar apical-medial contractile MyoII meshworks also play a critical role in controlling the apical area of epithelial cells: for example, in the developing fly notum and retina.^{14,24}

At the basal surface, epithelial cells are attached to a specialized extracellular matrix (ECM) called the basement membrane (BM). The BM provides mechanical and biochemical cues to support epithelial polarity and morphogenesis.^{25,26} The basal surface and its associated BM play major roles in shaping tissues.^{27–32} For example, tissue-wide basal contraction drives bending of the *Drosophila* wing epithelium.³³ Cell basal contraction is also essential for optic cup development³⁴ and formation of the midbrain-hindbrain boundary in zebrafish.^{35,36} In epithelial development, MyoII has been shown to power cell basal contraction. Basal surface contraction also requires integrin,

which mediates the adhesion of cells to the BM.^{37–39} This surface receptor is required for basal contraction during optic cup morphogenesis in medaka fish.^{40–42} Integrins also regulate cell shape in the *Drosophila* follicular epithelium³² and in the fly retina.⁴³ In the follicular epithelium, loss of integrins leads to defects in F-actin organization and to a reduction in cell basal surface area, suggesting that these adhesion receptors are required to counterbalance contractility of the basal MyoII cytoskeleton.³² In the retina, integrin adhesion is required to induce cell basal surface geometry remodeling, prior to contraction of this tissue surface.^{43,44} In this context, although both apical and basal surface regulation can contribute to shaping epithelial cells and tissues, we still lack a good understanding of how these regulations are coordinated between and across tissue surfaces to shape cells in 3D.

To examine how cells coordinate remodeling of their apical, lateral, and basal surfaces in morphogenesis, we used the *Drosophila* retina. This epithelium consists of ~750 repeating units called ommatidia. At the core of each ommatidium are eight photoreceptors that are topped by four glial-like cone cells that make up the lens of the eye. The cone cells are surrounded by two primary pigment cells, themselves surrounded by a hexagonal lattice of interommatidial cells (IOCs).⁴⁵ The IOCs include secondary and tertiary pigment cells, which meet each other basally to surround the photoreceptors' axons.⁴⁶ During morphogenesis, these cells acquire specific apical and basal geometries^{14,15,43,45–49} to shape the ommatidium as a hexagonal prism. Subsequently, the basal surface of the retina contracts, a morphogenetic step that is thought to induce curvature of the epithelium.⁴⁴ The retinal cells also expand their lateral membrane, elongating along the distal (lens) to proximal (brain) axis, to thicken the epithelium, essential for eye function.^{46,50}

Here, we combined intravital imaging, genetics, and a mathematical vertex model to investigate how retinal cells coordinate remodeling of their apical, lateral, and basal surfaces to form a functional visual system. Our findings indicate that retinal curvature stems from differential tissue surface growth and inside-out fluid pressure. Moreover, we show that uniform thickening of this curved epithelium requires coordination of cell basal contraction and cell elongation, a process that we find depends upon integrin and MyoII.

RESULTS

Basal contraction coincides with retinal thickening

To understand how tissue curvature, thickening, and contraction are related during retinal morphogenesis, we used light sheet microscopy to image retinas at different developmental stages. First, we quantified apical and basal surface lengths and retinal depth (Figures 1A–1E) from transverse optical sections of the retina. In these experiments, alternatively imaging fixed retinas or intravital retinas yielded the same results (Figure S1). We found that from 21 to 44 h after puparium formation (APF), the apical and basal tissue surfaces grew in length by 146 and ~141 μm, respectively, revealing a 3.5% difference in growth rate between these two surfaces (Figure 1E). Throughout this period, the basal surface was slightly shorter than the apical surface. Then, from 50 h APF, we found that the basal surface reduced from a mean of 427 μm in length to 276 μm as the

IOCs contracted their basal surfaces. This surface contraction was concomitant with an increase in retinal depth from 18 to 119 μm (Figure 1E). In contrast, the apical surface remained approximately the same length from 50 h APF to adult. This is likely due to lens secretion, which hardens the apical surface of the retina from 50 h APF.⁵¹ Because previous work proposed that basal contraction induces retinal curvature,⁴⁴ we next wanted to determine whether there was a correlation between these two processes. We measured the curvature of the apical and basal retinal surface at different developmental stages (Figures 1F and 1G). These measurements revealed that, *in vivo*, the retina was already almost fully curved by 44 h APF, before basal contraction had started (Figures 1F–1H). Therefore, retinal tissue curvature must be largely independent from tissue basal contraction. Instead, our results suggest that a small differential in apical and basal surface growth induces retinal tissue curvature. Moreover, our results raise the possibility that basal contraction and cell elongation are linked processes because they occur concomitantly.

Retinal curvature can be explained by a small differential in apical and basal surface lengths

To test the idea that a difference in apical and basal surface area may induce tissue curvature, we used a vertex model (Figure 2).⁵² We modeled the *Drosophila* retina by representing it as a cross-section along the proximal-distal axis, with each ommatidium described by a quadrilateral with an apical, basal, and two lateral edges (Figures 2A and 2B). We assumed that ommatidium shape is determined by four forces stemming from associated energies, which were the same across the retina: tension along the basal, apical, and lateral edges, modeled by Hookean springs with rest length zero and characterized by spring elasticities. The model also included an area force, characterized by a preferred area and an area elasticity. Because the absolute values of the elasticities only set the timescale, and we were interested in equilibrium shapes, it was enough to consider their ratios—effectively, we set the area elasticity to 1. This yielded four parameters per ommatidium: apical tension, basal tension, lateral tension, and preferred area. Initially, the retina was modeled as a flat sheet, where forces were in equilibrium (Figures 2D–2F). Using this as initial conditions, we explored which combination of parameters could induce the measured tissue curvature, striving, in the spirit of Occam's razor, to find the simplest possible explanation (Figure S2). We note that changing one parameter, either apical or basal tension, can give rise to a curve tissue (Figure S2).^{33,53,54} However, mathematical analysis of our model revealed that, if all ommatidia had the same properties, the initial curving to produce the *in vivo* retinal shape could not be explained by changing only one model parameter (Figures 2D and S2). Our quantification of retinal shape during development, from 0 to 50 h APF (Figure 1E), shows a 3.5% difference in growth rate between the apical and basal surface of the retina. Generating this differential requires different rates of relaxation between the apical and basal surfaces, with reductions of 73% and 70%, respectively, in the model (Figures 2E–2G), (for mathematical details, see Methods S1). Altogether, consistent with our *in vivo* measurements of apical and basal surface development, our computational approach

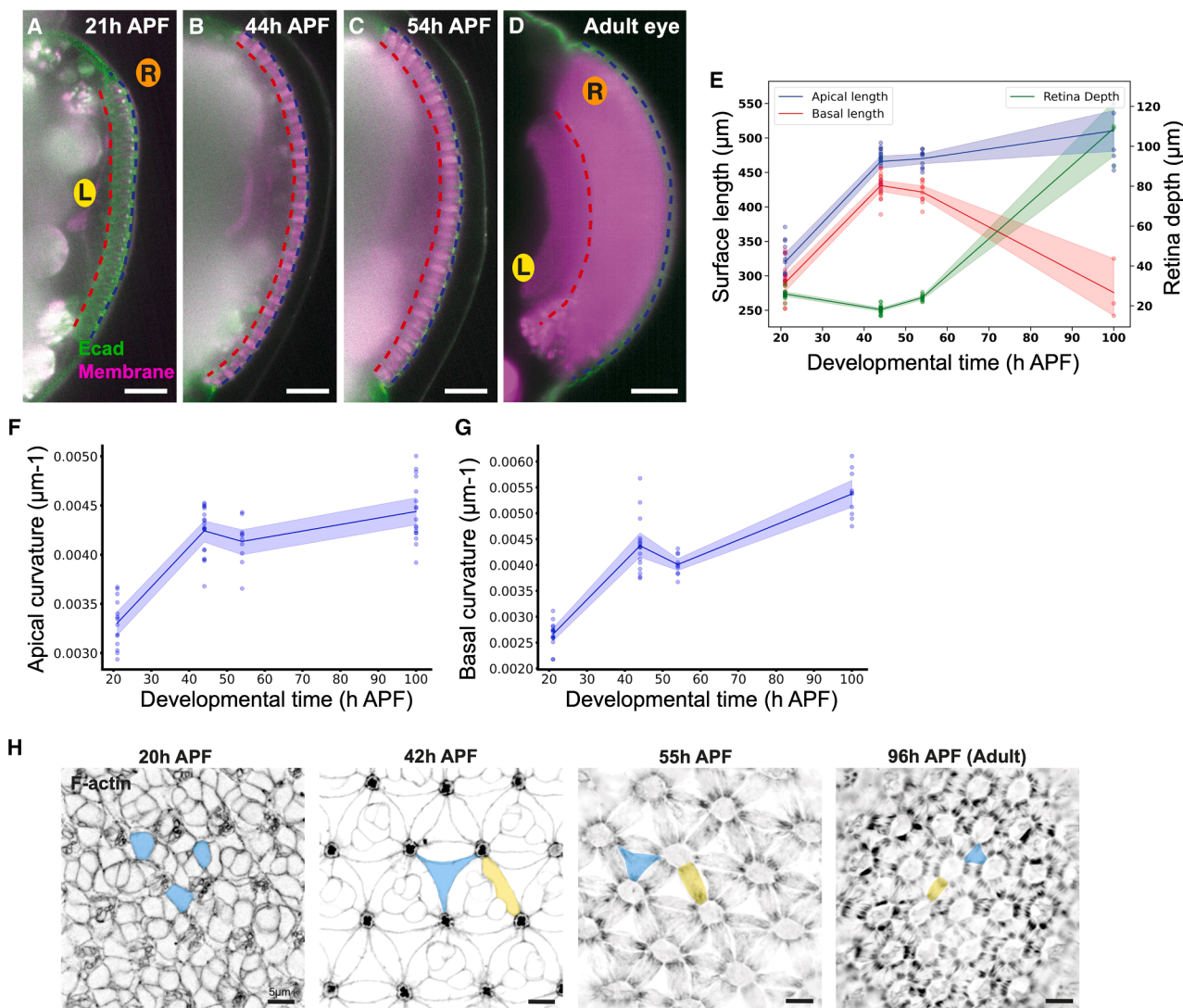


Figure 1. Basal contraction coincides with retinal thickening

(A–D) Light sheet optical sections of retinas at 21, 44, and 54 h APF and adult. Ecad:GFP in green and Myr:RFP in magenta. R, retina; L, lamina. Scale bar, 50 μ m. (E) Measurements of apical length (blue), basal length (red), and retinal depth (green) at the developmental stages shown in (A)–(D). Each scatter point represents one retina measurement, and the shaded area shows the 95% confidence interval. n (21 h retina) = 15, n (44 h retina) = 17, n (54 h retina) = 10, n (adult retina) = 3. (F) Measurements of apical curvature at the developmental times shown in (A)–(D). Each scatter point represents one retina measurement, and the shaded area shows the 95% confidence interval. n (21 h retina) = 14, n (44 h retina) = 19, n (54 h retina) = 10, n (adult retina) = 17. (G) Measurements of basal curvature at the developmental times shown in (A)–(D). Each scatter point represents one retina measurement, and the shaded area shows the 95% confidence interval. n (21 h retina) = 15, n (44 h retina) = 17, n (54 h retina) = 10, n (adult retina) = 10. (H) Confocal optical sections of the retinal basal surface at 20, 42, 55, and 96 h APF stained with phalloidin to visualize F-actin. Blue overlay highlights a single tertiary pigment cell, and the yellow overlay highlights a single secondary pigment cell. Scale bar, 5 μ m.

See also Figure S1.

suggests that a small differential in apical and basal surface expansion can lead to curvature.

Fluid pressure plays a key role in shaping the retina

Although differential surface expansion provides a potential mechanism for tissue curvature, we also noted that, upon dissection, retinal curvature was often lost. This observation suggested that regulations extrinsic to the retinal epithelium might have a role in shaping the retina. The developing pupa

contains fluid, analogous to a fluid-filled sack, and we hypothesized that fluid pressure might play a role in promoting retinal tissue curvature. To test this idea, we punctured the posterior end of the pupae using a needle, so as to not damage the retina but to drain a small volume of liquid from the pupae (Figure 2H). These perturbation experiments consistently induced retinal deformations, including curvature inversion (Figures 2I and 2J). Based on these findings, we conclude that the early pupal retina behaves as a flexible material and that internal fluid pressure

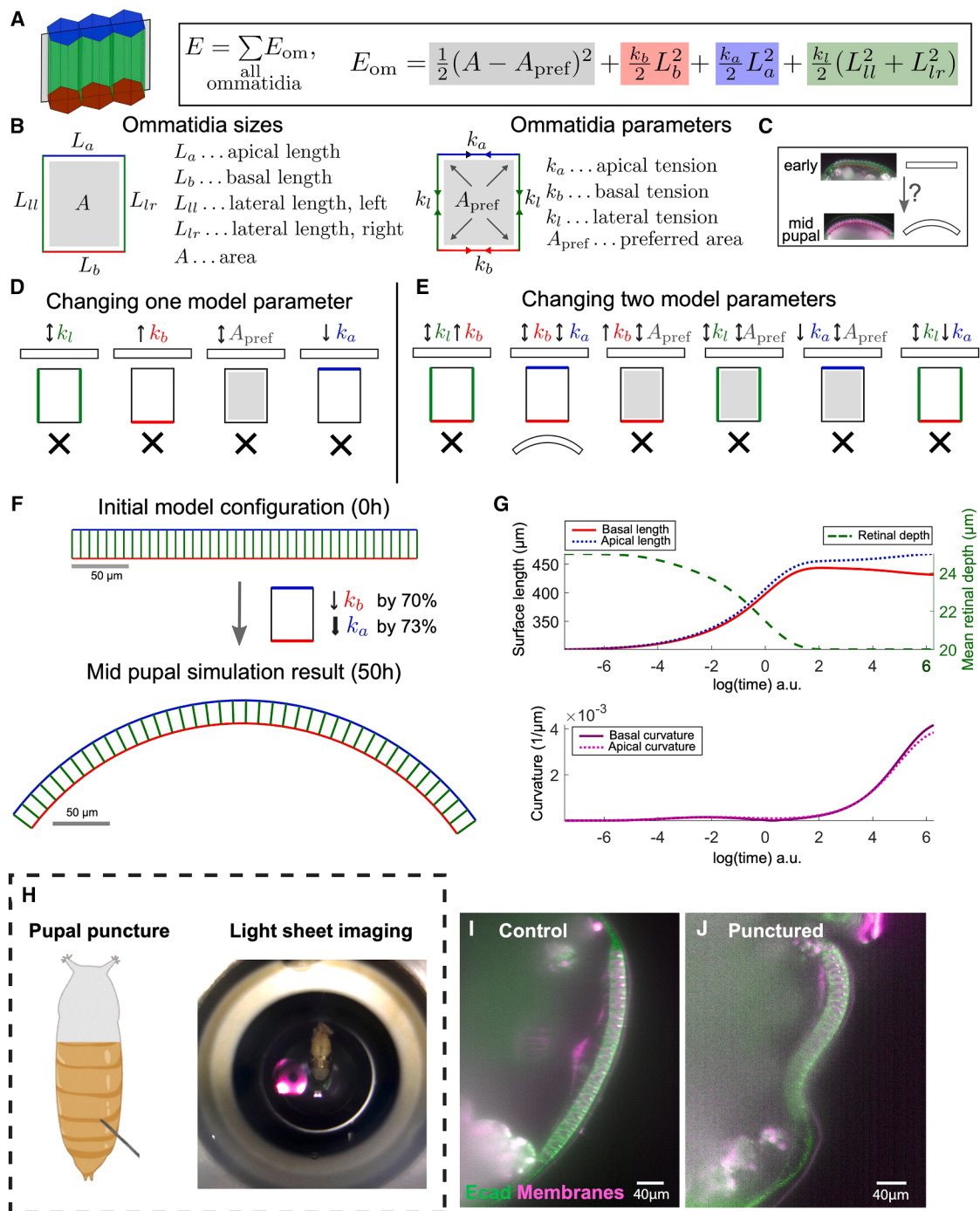


Figure 2. Vertex model of retinal morphogenesis simulating early retinal tissue curvature

(A and B) Vertex model of retinal morphogenesis.

(A) Equation for the total and per ommatidium energy that is being minimized.

(B) Schematics and explanation of relevant model quantities and parameters per ommatidium.

(C) Schematic of morphogenetical changes to be explained between early and mid-pupal stage.

(D and E) Schematic summary of single (D) and double (E) model parameter changes; parameter changes are represented by color and arrow direction. Shapes above and below the small schematic ommatidia represent initial and final shapes, bold crosses mark unsuccessful parameter changes that do not match the biology.

(F) Top: simulation result (equilibrated) at 0 h that gives an exact match with the biological data for early development; apical sides marked in blue, basal sides marked in red, and lateral sides marked in green. Bottom: simulation result (equilibrated) at 50 h that gives an exact match with the biological data at the mid-pupal

(legend continued on next page)

plays an important role in shaping this epithelium during early development.

Coordination of basal contraction and cell growth is required to shape the *Drosophila* retina as a dome

After curvature has been established, the retinal epithelium undergoes concomitant basal surface contraction and thickening (Figure 1E), suggesting that these processes are coordinated. To explore this possibility, we used our vertex model. After the initial bending of the retina from 0 to 50 h APF, the lens is secreted.⁵⁵ This creates a hard surface that does not allow for further apical deformations. Therefore, we fixed the apical vertices in our model. Consequently, the number of model parameters was reduced from four to three per ommatidium: basal tension, lateral tension, and preferred area. From 50 h APF to adult, the basal surface of the retina reduced in length from ~427 to ~276 μm, and this was concomitant with a drastic increase in retinal depth from 18 to 119 μm (Figures 1A–1E). Here, we explored the forces that might underpin these biological data.

Because it was not possible to reproduce all biological measurements exactly, we defined an error that quantified the difference in simulated and measured retinal shape to identify the most likely scenarios (Figure S3A). We found that changing only one model parameter, i.e., increasing basal tension; decreasing lateral tension, which leads to cell elongation; or increasing preferred area leading to cell growth alone could not produce the adult shape of the retina (Figures S3B and S3D–S3L). These single parameter changes gave error values of 0.32, 0.89, and 0.36 at best for changes in basal tension, preferred area, and lateral tension, respectively. Changing one parameter could not recapitulate the basal length and retinal depth we measured in retinal development (Figures S3D–S3F). Furthermore, increasing basal tension or increasing preferred area in the model did not produce the biological retinal curvature (Figures S3G and S3H). Decreasing lateral tension led to the biological basal curvature, but the final shape of the retina lacked the depth observed in the biological data (Figures S3I and S3L). One interesting finding from these results was that reducing lateral tension led to a drastic decrease in basal surface length without a need for increasing basal tension (Figure S3F). However, in this simulation, we observed that the distribution of cell lengths across the retina became heterogeneous, with the outer cells having small basal lengths (Figure S3L). This is not what we observed in retinal development. Therefore, shaping the retinal epithelium likely requires changes in two or more force parameters.

We then explored which combination of changes in two force parameters could generate the shape of the adult retina. We found two possible paths of changing forces that yielded a

similarly good match with the observed dome-like shape of the retina (Figure 3). One way was to reduce lateral tension, and hence grow laterally, while also increasing the preferred area of cells. In this scenario, basal tension remained the same as the parameters that produced the 50 h APF retina in the model (Figure 2). Examining the temporal dynamics of this simulation revealed that the retina initially thickened on its periphery before the basal surface length began to reduce to shape the retina (Figures 3B and 3D). Therefore, it is theoretically possible to produce the adult shape of the retina without increasing basal tension. Importantly, this also revealed that increasing the depth of the curved retina in a uniform manner could not occur without reducing the basal surface of the retina. In the second scenario, producing the adult retina was achieved when basal tension and preferred area were increased together (Figure 3C). Increasing basal tension in the model led to a gradual reduction of the tissue basal surface that resembled the biological data (Figures 1E, 1F, and 3E). In any case, our simulations indicate that a combination of cell growth, basal surface contraction, or modulation of lateral tension drives tissue thickening.

Retinal cell growth drives tissue thickening

Our computational model calls for a 4.5-fold increase in cell growth. To explore this growth parameter, we measured the growth rates of the retinal cells. To this end, we segmented retinal cells at three different developmental stages, 24, 36, and 72 h APF (Figure 4), and estimated the volume of the developing ommatidium. Using this approach, we found that ommatidial volume increased by 4.97-fold between 36 and 72 h APF (Figures 4A and 4B). Notably, this growth occurred primarily along the lateral, proximal-distal axis of the ommatidium (Figure 4A). We next analyzed the growth rates of individual cell types. Between 36 and 72 h APF, the secondary and tertiary pigment cells, which form the hexagonal lattice of the ommatidium, exhibited a 7.4-fold increase in volume (Figures 4C and 4D). Similarly, the photoreceptors, located at the core of the ommatidium, grew by 7.3-fold (Figures 4E and S4). In contrast, the two primary pigment cells, which span only the apical region, showed a more modest growth of 2.6-fold (Figure 4F). The cone cells could not be fully segmented at 72 h APF, but they appeared to grow less than other cell types during development (Figure S4). These results show that interommatidial and photoreceptor cells have the highest growth rates, with growth occurring preferentially along the apical-basal axis of the tissue, suggesting that these cells drive tissue thickening.

To further assess the relationship between cell growth and tissue thickening, we took advantage of mutations in the *PTEN* locus. As previously reported, whole mutant retinas for *PTEN* were significantly larger than the wild type (Figure S5).⁵⁶ Light sheet microscopy showed that apical length, basal length, and retinal

stage, colors as in up. Model parameters between the 0-h and the 50-h prediction differ in the basal tension (reduced by 70%) and the apical tension (reduced by 73%).

(G) Time evolution of simulated quantities (up: basal and apical length and retinal depth; down: basal and apical curvature). For details on parameter values and (computational) method, see Methods S1.

(H) Experimental setup: puncturing pupae at the posterior body and imaging on a light sheet microscope immediately.

(I and J) Light sheet optical section of a retina that was not punctured and a retina that had been punctured, respectively. Ecad in green and myristoylated RFP to label cell membranes in magenta. Scale bar, 40 μm.

See also Figure S2 and Methods S1.

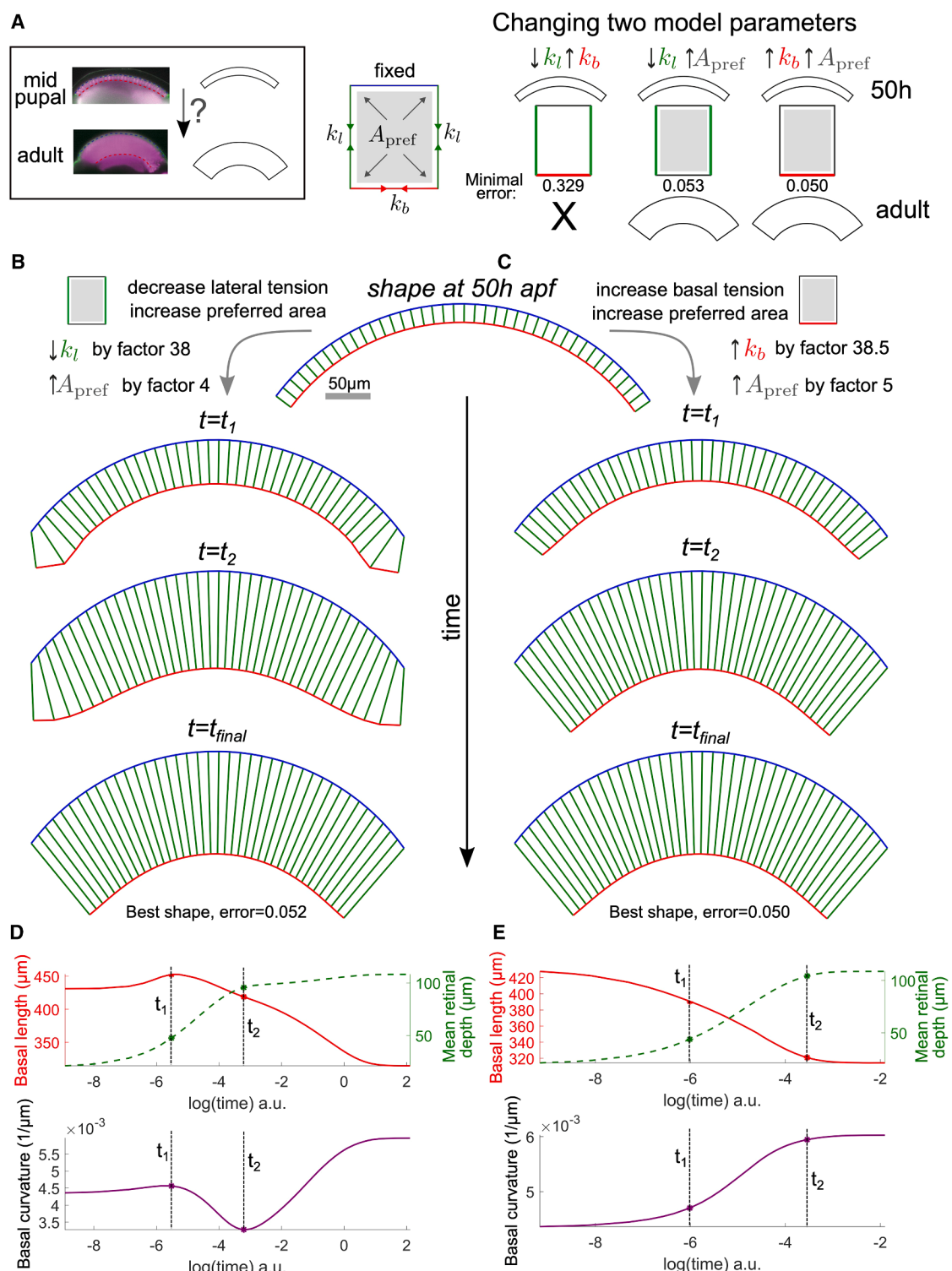


Figure 3. Basal surface reduction is required for retinal tissue thickening

(A) Left: schematic of morphogenetical changes to be explained between mid-pupal and adult stage. Right: schematic summary of double model parameter changes, colors, etc. as in Figures 2D and 2E. Minimal error achieved written below.

(B and C) Simulation snapshots at different time points (also marked below in D and E) for parameters that minimize the error defined in Figure 2A for decreasing lateral tension and increasing preferred area (B) and increasing basal tension and increasing preferred area (C).

(legend continued on next page)

depth all increased in *PTEN*-mutant retinas compared with wild type (Figure S5). Assessing relative surfaces lengths by calculating a ratio between the apical and basal lengths and between apical length and retinal depth showed that the length ratios were maintained (Figures S5F, S5G, S5M, and S5N). Modeling the *PTEN* loss-of-function genotype by increasing the target area of the computational ommatidium could also recapitulate the shape of the adult retina, further validating the computational model (Figure S5O). Altogether, these findings are consistent with the hypothesis that retinal cell growth is a key driver of tissue thickening.

The IOCs and photoreceptors appear to contribute the most to retinal tissue growth, suggesting that both cell types promote tissue thickening (Figure 4). To decipher whether both cell types contribute to tissue thickening, we inhibited the expression of the transmembrane protein Crumbs (*crb*), which is required for photoreceptor elongation along the proximal-distal axis of the retina.^{57,58} To do this, we used the *crb*^{11A22} null allele.⁵⁹ As expected, in *crb*^{11A22} mutant retinas, photoreceptors failed to elongate (Figures 5A and 5B). In these retinas, basal length was longer than in control retinas, with a mean basal length of 320 μm compared with 254 μm in control retinas (Figure 5E). The apical length also increased, with a mean of 588 μm compared with 520 μm in control retinas (Figure 5F). These results are consistent with previous work showing that *crb*-mutant eyes contain more ommatidia and are, therefore, larger than the wild type.⁶⁰ Importantly, we did not measure any difference in retinal tissue thickness compared with controls (Figure 5G). In the absence of *crb*, the IOCs contracted their basal surface as in wild-type control retinas, indicating that photoreceptor elongation and basal surface contraction are independent processes (Figures 5J and 5K). From these experiments, we conclude that photoreceptor elongation is dispensable for retinal tissue thickening. Altogether, these results suggest retinal tissue thickening is promoted by the IOCs.

The basal surface of retinal cells is under tension

Our computational approach indicates that either decreasing lateral tension or, alternatively, increasing basal tension can lead to uniform thickening of the curved retina. To decipher the differences between these alternative simulations, we used genetics to perturb contraction and performed laser ablations to estimate tension forces at the basal surface of retinal cells.

MyoII is localized at the basal surface of contracting retinal cells (Figures 6A–6C), where it has been implicated in surface contraction.⁴⁴ To inhibit MyoII, we used a dominant-negative MyoII transgene, YFP-myosinII-DN (MyoII-DN).⁶¹ In cells expressing this transgene, we found that F-actin was disorganized compared with wild-type cells, and cells failed to contract basally (Figures 6D–6G). We then expressed MyoII-DN in all retinal cells with the GMR-Gal4 strain and used light sheet microscopy to image the corresponding retinas (Figure 6H). We found this did not affect apical surface curvature (Figure S6A). However, it led to an increase in both apical and basal surface length

compared with wild-type retinas, with an average basal length of 414 μm compared with 273 μm in control retinas (Figures 6I and S6B). Retinal depth was also reduced in these retinas, with an average depth of 77 μm compared with 103 μm in control retinas (Figure 6J). From this, we conclude that MyoII is required for limiting the expansion of the apical surface, as well as for cell basal contraction and elongation along the apical-basal axis of the retina.

Next, to estimate basal tension, we performed laser ablations at 42 h APF (before contraction) and 65 h APF (during contraction) on retinas expressing Utrophin::GFP to visualize F-actin, focusing on the IOCs (Figures 6K and 6L). At 42 h APF, the initial recoil over the first time point and total cell edge displacement over 118 s was, on average, 0.0911 μm/s and 1.6 μm, respectively (Figures 6K, 6K', 6M, and 6N; Video S1). At 65 h APF, during basal contraction, initial recoil over the first time point and total cell edge displacement over 118 s was, on average, 0.4018 μm/s and 1.15 μm, respectively (Figures 6L–6N; Video S2). The increase in initial recoil from 42 to 65 h APF is consistent with these cells undergoing basal contraction. We note the total cell edge displacement over the time frames measured was higher at 42 h APF (before contraction) than at 65 h APF (during contraction), indicating that the basal surface of the retina becomes more stable as it undergoes contraction. From these results, we conclude that the basal surface undergoes MyoII-dependent contraction during retinal tissue thickening.

Integrin is required for both cell basal contraction and elongation

To complement our genetic experiments targeting MyoII, and to further examine the relationship between cell basal contraction and elongation, we targeted integrins. First, we expressed a dominant-negative β-PS integrin (Mys^{DN}) in all retinal cells using the GMR-Gal4 driver (Figure S7A). This version of the β-PS sub-unit of integrin does not enable integrin-BM adhesion but retains signaling capability.⁶² Expressing Mys^{DN} did not affect apical curvature or apical surface length (Figures S8A and S8B). However, it resulted in an increase in basal surface length with a mean of 392 μm compared with 276 μm in wild-type control retinas (Figure S7B). It also resulted in a decrease in retinal depth, with a mean retinal depth of 70 μm compared with 109 μm in wild-type control retinas (Figure S7C). Second, we used RNAi to inhibit the expression of talin, which is an essential component of the integrin adhesion complex (Figure S7D).⁶³ Expressing talin RNAi did not affect apical curvature or apical surface length (Figures S8C and S8D). However, it led to an increase in basal surface length, with a mean of 440 μm compared with 260 μm in wild-type control retinas (Figure S7E). In these retinas, retinal depth reduced, with a mean of 70 μm compared with 110 μm in wild-type control retinas (Figure S7F). Third, we made use of the Gal80TS system⁶⁴ to specifically inhibit talin after 50 h APF so that prior patterning of the retinal basal surface⁴³ would not be affected by this knockdown (Figure 7). We confirmed the

(D and E) Top: time course of simulated basal length (left y axis, red-solid) and mean retinal depth (right y axis, green-dashed) for decreasing lateral tension and increasing preferred area (D) and increasing basal tension and increasing preferred area (E). Vertical dashed lines mark time points corresponding to simulation snapshots in (B) and (C). Bottom: as above, but for simulated basal curvature. For details on parameter values and computational methods, see Methods S1. See also Figure S3 and Methods S1.

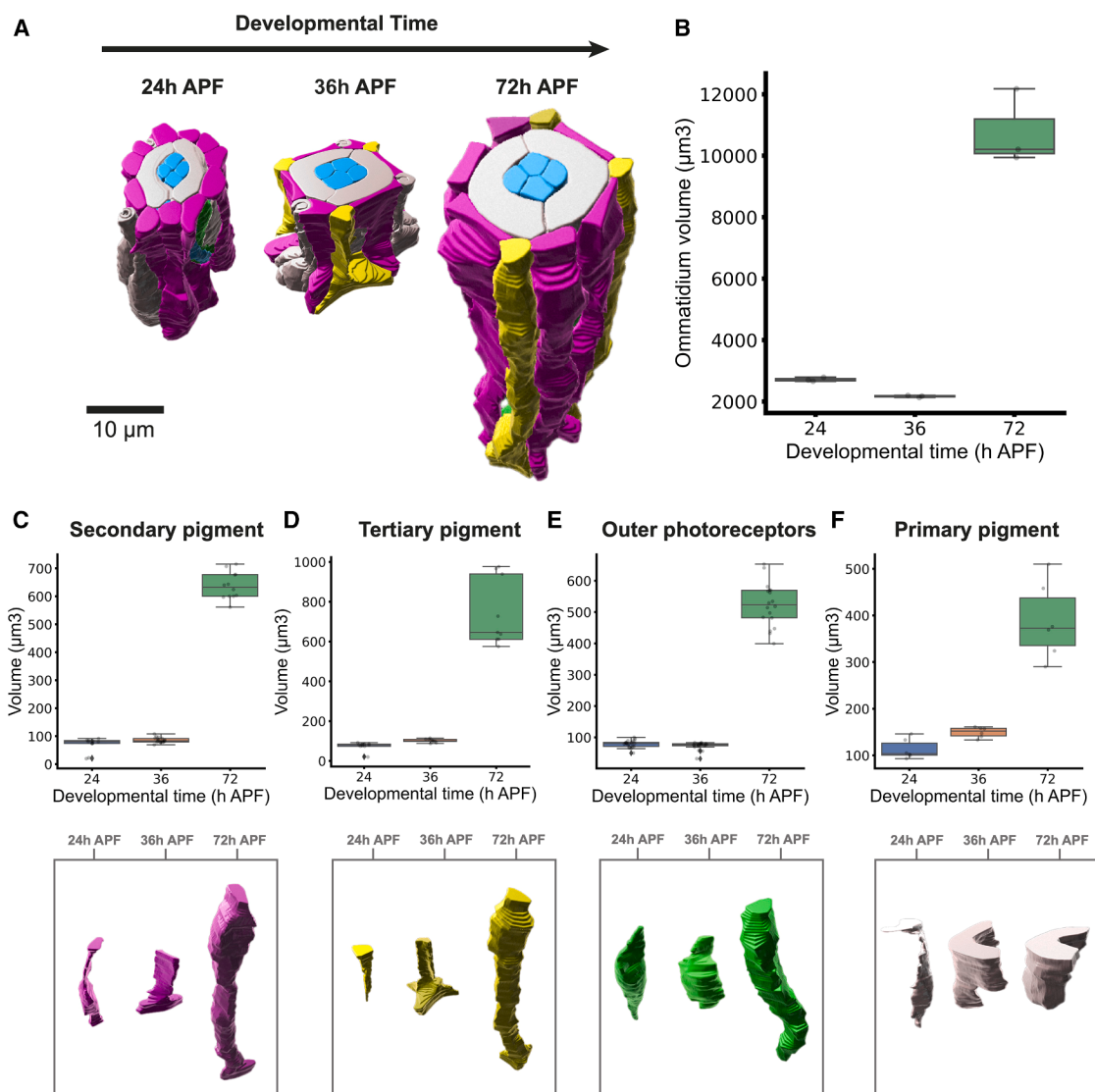


Figure 4. Retinal cell growth drives tissue thickening

(A) 3D segmented ommatidia at different developmental stages from 24, 32, and 72 h APF. Cone cells are in blue, primary pigment cells in gray, tertiary pigment cells in yellow, and secondary pigment cells in pink. At 24 h APF, interommatidial cells are all in pink because their fate cannot be labeled from cell shape. Scale bar, 10 μm.

(B) Quantification of ommatidial volume at corresponding developmental stages shown in (A).

(C–F) Cell volumes and representative 3D segmented cells underneath at 24, 36, and 72 h APF for secondary pigment cells (C), tertiary pigment cells (D), outer photoreceptors (E), and primary pigment cells (F). Three ommatidia from three different retinas were quantified for each condition.

See also Figures S4 and S5.

retinas were not affected before being shifted to the permissible temperature (Figure S9). In these retinas, we did not measure any significant effects in apical curvature or apical surface area (Figures S8E and S8F). However, we measured a decrease in basal surface contraction when compared with control retinas (Figures 7A and 7B) as well as a reduction in retinal depth (Figures 7A–7C).

Integrins mediate cell basal adhesion, raising the possibility that failure in tissue thickening could be a result of cell detachment and recoil from the BM, rather than being a direct consequence of a failure in basal contraction. To examine this

possibility, we imaged retinas from animals expressing GFP-tagged collagenIV (Viking::GFP),⁶⁵ a key BM protein, when *talin* was knocked down in all retinal cells. We found the basal surface of the retina remained apposed to the BM when inhibiting integrin adhesion (Figures 7D–7E'). Therefore, detachment and recoil from the BM does not seem to account for the tissue shortening we observe.

Finally, to complement these genetic experiments, we modeled the relationship between tissue basal contraction and thickening (Figure 7F). Here, we simulated our experimental perturbations of basal contraction by reducing basal tension, using

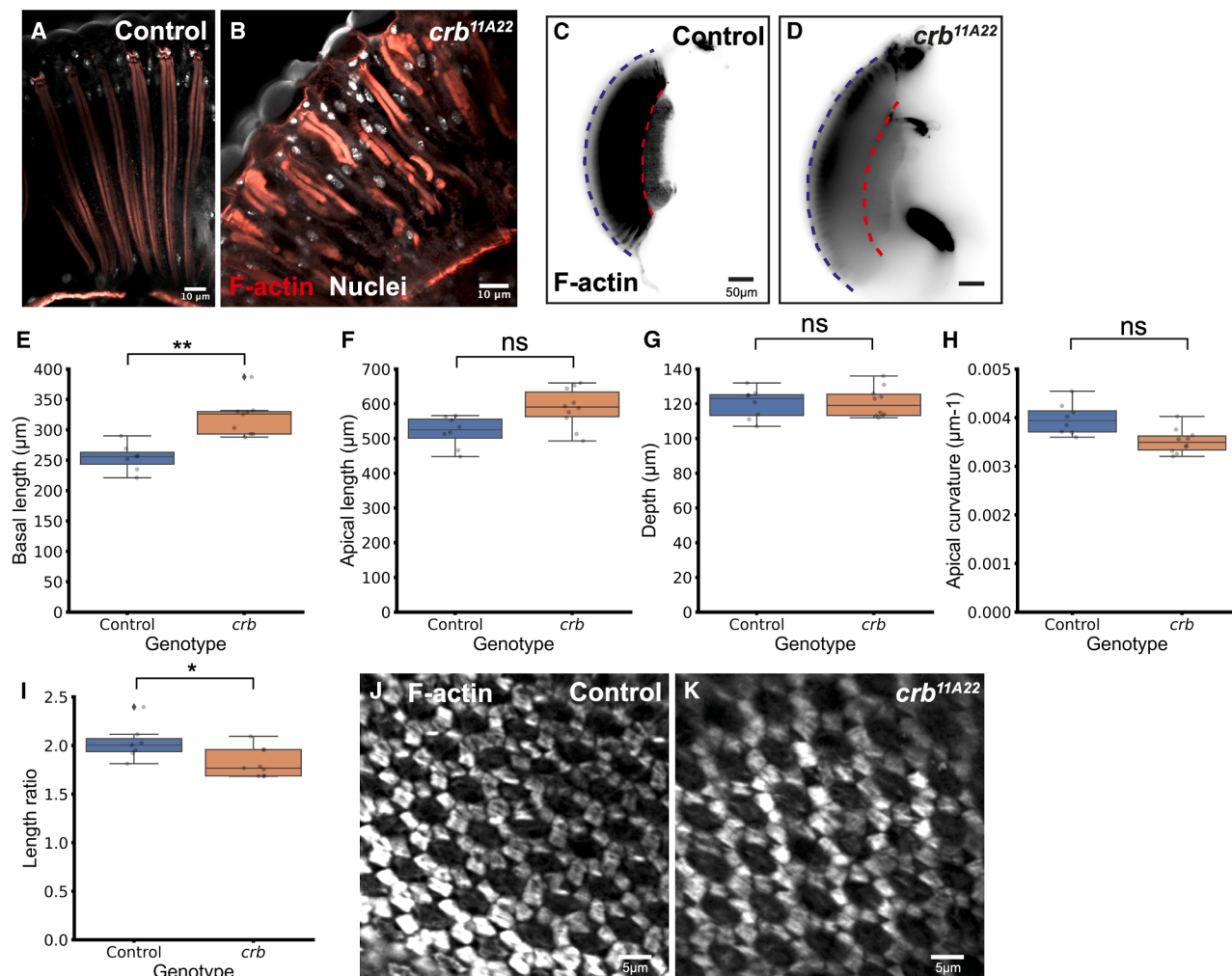


Figure 5. Photoreceptor elongation is not required for retinal tissue thickening

- (A) Confocal section of a control retina with phalloidin/F-actin in red and nuclei in gray. The top of the section shows the lens surface, and the bottom is the basal surface where interommatidial cells contract. The dense red structures running the length of the retina are rhabdomeres, which contain the light-sensitive pigments of the retina. Scale bar, 10 μm.
- (B) Confocal section of a *crb*-mutant retina (*crb*^{11A22}) with phalloidin/F-actin in red and nuclei in gray.
- (C) Light sheet optical section of a control retina. Blue dotted line represents the apical surface, and the red dotted line represents the basal surface. Scale bar, 50 μm.
- (D) Light sheet optical section of a *crb*-mutant retina. Blue dotted line represents the apical surface, and the red dotted line represents the basal surface. Scale bar, 50 μm.
- (E) Quantification of retinal basal length. $n = 7$ control retinas, $n = 8$ *crb*-mutant retinas.
- (F) Quantification of apical length. $n = 8$ control retinas, $n = 10$ *crb*-mutant retinas.
- (G) Quantification of retinal depth. $n = 8$ control retinas, $n = 10$ *crb*-mutant retinas.
- (H) Quantification of apical curvature. $n = 8$ control retinas, $n = 10$ *crb*-mutant retinas.
- (I) Quantification of length ratio, apical/basal length. $n = 7$ control retinas, $n = 8$ *crb*-mutant retinas.
- (J and K) Confocal optical section of the basal surface of a control and a *crb*-mutant retina. Phalloidin is in gray to label F-actin. Scale bar, 5 μm. All statistics tests Mann-Whitney U. ns, $p > 0.05$; * $p \leq 0.05$, ** $p \leq 0.01$, *** $p \leq 0.001$.

the early curved retinal epithelium at 50 h APF as the starting point. When basal tension was reduced in the model, the simulated retina had a longer basal surface and reduced retinal depth, which recapitulates the phenotypes we observed when inhibiting MyoII activity and integrin expression. Altogether, these results indicate that cell basal contraction and elongation along the apical-basal axis of the retina are coupled processes and that integrins and MyoII play an essential role in this coupling.

DISCUSSION

Shaping a tissue in 3D requires the coordination of morphogenetic processes between the apical, lateral, and basal axes of cells and tissues. However, the mechanisms and pathways that enable this coordination are poorly understood. Here, we investigated the morphogenetic axes involved in shaping the fly retina as a dome-like structure. Our work reveals three novel

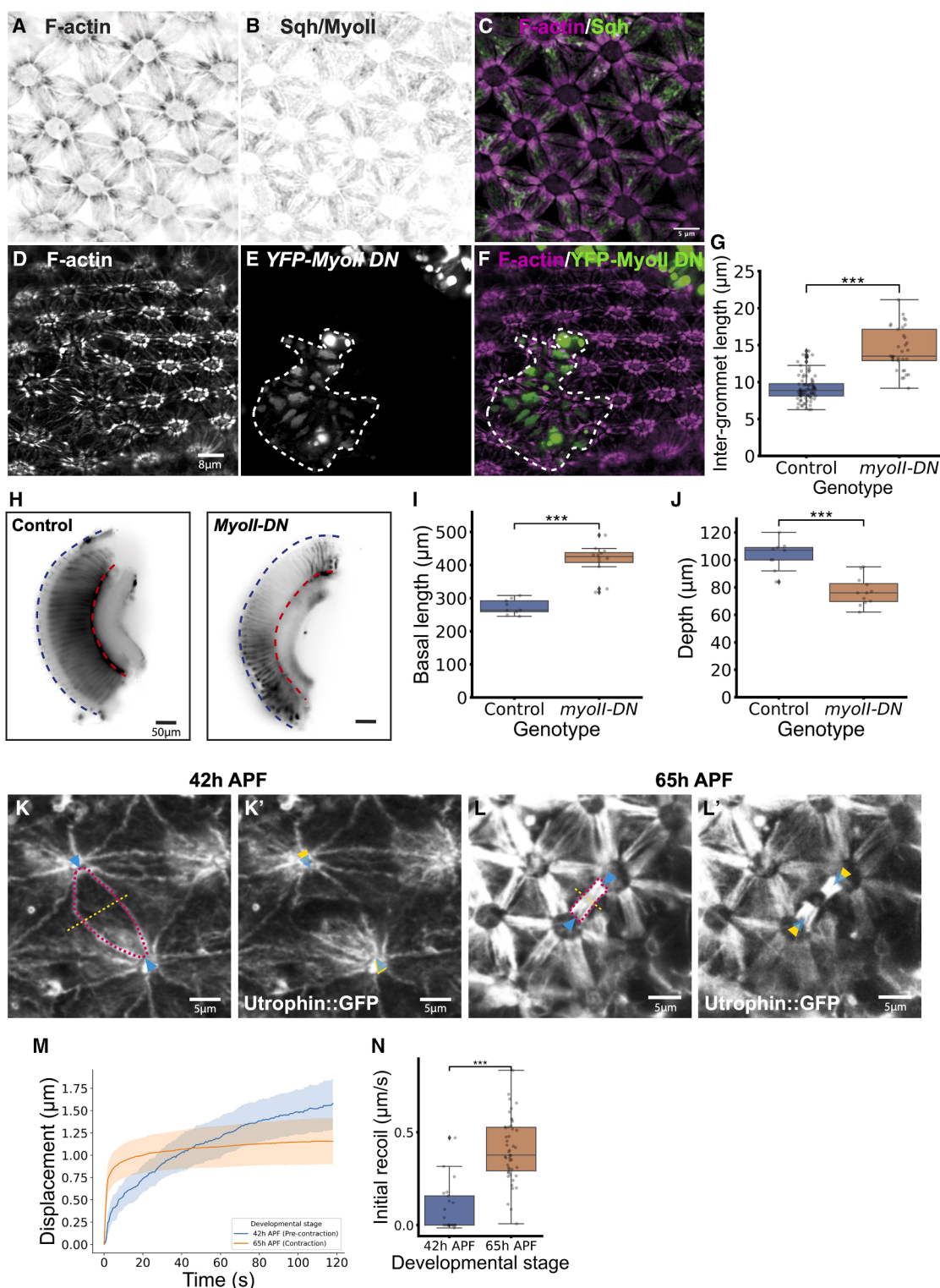


Figure 6. The basal surface of the retina undergoes MyoII-dependent contraction

(A and B) Confocal section of the retinal basal surface at 55 h APF labeled with phalloidin to visualize (A) F-actin and (B) sqh:myoII::GFP to visualize non-muscle myosin.

(C) Merged images of F-actin in magenta and sqh:GFP in green. Scale bar, 5 μ m.

(D) Confocal section of the retinal basal surface at 72 h APF labeled with phalloidin to visualize F-actin. Scale bar, 5 μ m.

(E) MyoII-DN-expressing cells are marked with GFP and highlighted with a dotted line.

(legend continued on next page)

principles of epithelial morphogenesis. First, we demonstrate that a small differential in the lengths of the apical and basal surfaces, arising as these surfaces are growing at different rates, is theoretically sufficient to drive tissue curvature. Second, we present evidence that hydrostatic pressure can also play a critical role in promoting tissue curvature *in vivo*. Third, we show that the uniform thickening of a curved tissue like the retina requires the coordination of cell basal surface contraction and elongation along the apical-basal axis of the tissue. Our results argue that integrins and MyoII are central to this coordination process.

Mechanisms of tissue curvature

Many epithelia become curved during morphogenesis. This is, for example, the case for the vertebrate optic cup and for the *Drosophila* wing epithelium.^{33,34,41,42} For these developing tissues, curvature has been shown to be induced as the tissue basal surface contracts, a process that is powered by MyoII.^{33,34} Previous discussions on the mechanisms of retinal curvature in *Drosophila* have presented basal surface contraction as a driver of curvature.⁴⁴ Testing this idea experimentally, using light sheet microscopy, shows this cannot be the case—basal surface contraction occurs after the tissue is already curved. Our results, instead, argue that a small differential in apical and basal surface length, arising early in retinal tissue morphogenesis at a time when both surfaces undergo expansion, might contribute to inducing curvature. This conclusion is supported by our biological measurements and by our computational model. We note that computational approaches have previously shown that manipulating tension at one tissue surface, apical or basal, can induce curvature.^{33,53,54} We find this to be true for a tissue that does not expand—our vertex model can induce curvature in a flat tissue by changing either apical or basal tension. However, when simulating the early phase of retinal curvature when both tissue surfaces expand, our biological measurements are best recapitulated when we apply different apical and basal relaxation rates. Therefore, the computational model indicates that, in a growing tissue, a small differential in surface expansion rates, in this case 3%, can increase curvature. This matches well with our *in vivo* measurements revealing a 3.5%

difference in growth rates between the apical and basal surfaces of the retina. Based on these results, we envisage a small differential in tissue surface growth rate promoting curvature of the early developing retina. Our results also show that hydrostatic pressure also plays a role in this process. It will be interesting to better understand whether and how hydrostatic pressure and tissue surface expansion rates might be linked.

Mechanisms of curved tissue thickening

Altogether, our experiments suggest that, in a curved tissue like the retinal epithelium, basal surface contraction and cell elongation, fueled by cell growth, need to be coordinated to induce uniform tissue thickening. When parameter space was explored in the computational model, it revealed two scenarios that could produce the shape of the adult retina: (1) increasing retinal growth and reducing lateral tension and (2) increasing retinal growth and increasing basal tension. In scenario (1), basal surface reduction is passive and does not necessarily require an increase in basal tension. Interestingly, this mode of tissue thickening, promoted by a relaxation of cell lateral tension, has been proposed to promote thickening of the zebrafish retina.⁶⁶ In contrast to this situation, our work in the fly retina indicates that tissue thickening follows scenario (2), and it is induced through a combination of oriented cell growth and cell basal contraction. We also find that scenario (2), with increased basal tension, best recapitulates the biological process and parameters, including the initial recoil we measured upon cutting the basal surface of retinal cells. Moreover, inhibiting integrins, which are required for cell basal contraction in several tissues,^{33,41,44} also prevents cell elongation, leading to a thinner retina. Our examination of the relationship between the BM and the basal surface of the retina shows that the integrin-deficient retinal cells do not recoil from the BM; their basal surface remains apposed to the BM. Altogether, we therefore favor a model whereby basal regulation is required for cell elongation in tissue thickening.

Next to integrins, MyoII is also required for cell basal contraction and elongation. We note that inhibiting MyoII activity also led to an expansion of the apical surface of the retina. This result is

(F) Merged images of (D) and (E), F-actin in magenta and MyoII-DN cells in green.

(G) Measurements of inter-grommet distance for wild-type and MyoII-DN tissue. Each scatter point represents one inter-grommet measurement. Unpaired t test, *** $p \leq 0.001$. $n = 4$ retinas, $n = 85$ wild-type measurements, $n = 32$ MyoII-DN measurements.

(H) Optical sections from light sheet microscopy of retinas expressing MyoII-DN in all retinal cells with the GMR driver. On the right is a wild-type control retina. Scale bar, 50 μm .

(I) Quantification of basal surface length in MyoII-DN retinas compared with wild-type control retinas. Unpaired t test, *** $p \leq 0.001$. $n = 15$ retinas and $n = 9$ retinas for MyoII-DN and wild-type retina, respectively.

(J) Quantification of retinal depth in MyoII-DN retinas compared with wild-type control retinas. Unpaired t test, *** $p \leq 0.001$. $n = 15$ retinas and $n = 9$ retinas for MyoII-DN and wild-type retina, respectively. $n = 12$ retinas and $n = 10$ retinas for MyoII-DN and wild-type retina, respectively.

(K) Confocal section of a retinal basal surface at 42 h APF prior to ablation. Utrophin::GFP labels F-actin. A yellow line shows the region of interest (ROI) for ablation and blue arrows show the edges of the cells that are analyzed. Dotted red line shows a secondary cell basal profile. Scale bar, 5 μm .

(K') Post-ablation image after 118 s of imaging. Blue arrows represent the pre-ablation cell edge position, yellow arrows represent the post-ablation cell edge position.

(L) Confocal section of a retinal basal surface at 65 h APF prior to ablation. Utrophin::GFP labels F-actin. A yellow line shows the ROI for ablation and yellow arrows show the edges of the cells analyzed. A dotted red line shows a secondary cell basal profile. Scale bar, 5 μm .

(L') Post-ablation image after 118 s of imaging. Blue arrows represent the pre-ablation cell edge position, yellow arrows represent the post-ablation cell edge position.

(M) Quantification of cell edge displacement. 42 h APF: $n = 7$ retinas, $n = 21$ ablations. 65 h APF: $n = 19$ retinas, $n = 54$ ablation measurements. The shaded areas show the standard deviation.

(N) Initial recoil plot with each point representing an individual ablation measurement. 42 h APF: $n = 7$ retinas, $n = 21$ ablations. 65 h APF: $n = 19$ retinas, $n = 56$ ablation measurements. Mann-Whitney U, *** $p \leq 0.001$.

See also Figure S6 and Videos S1 and S2.

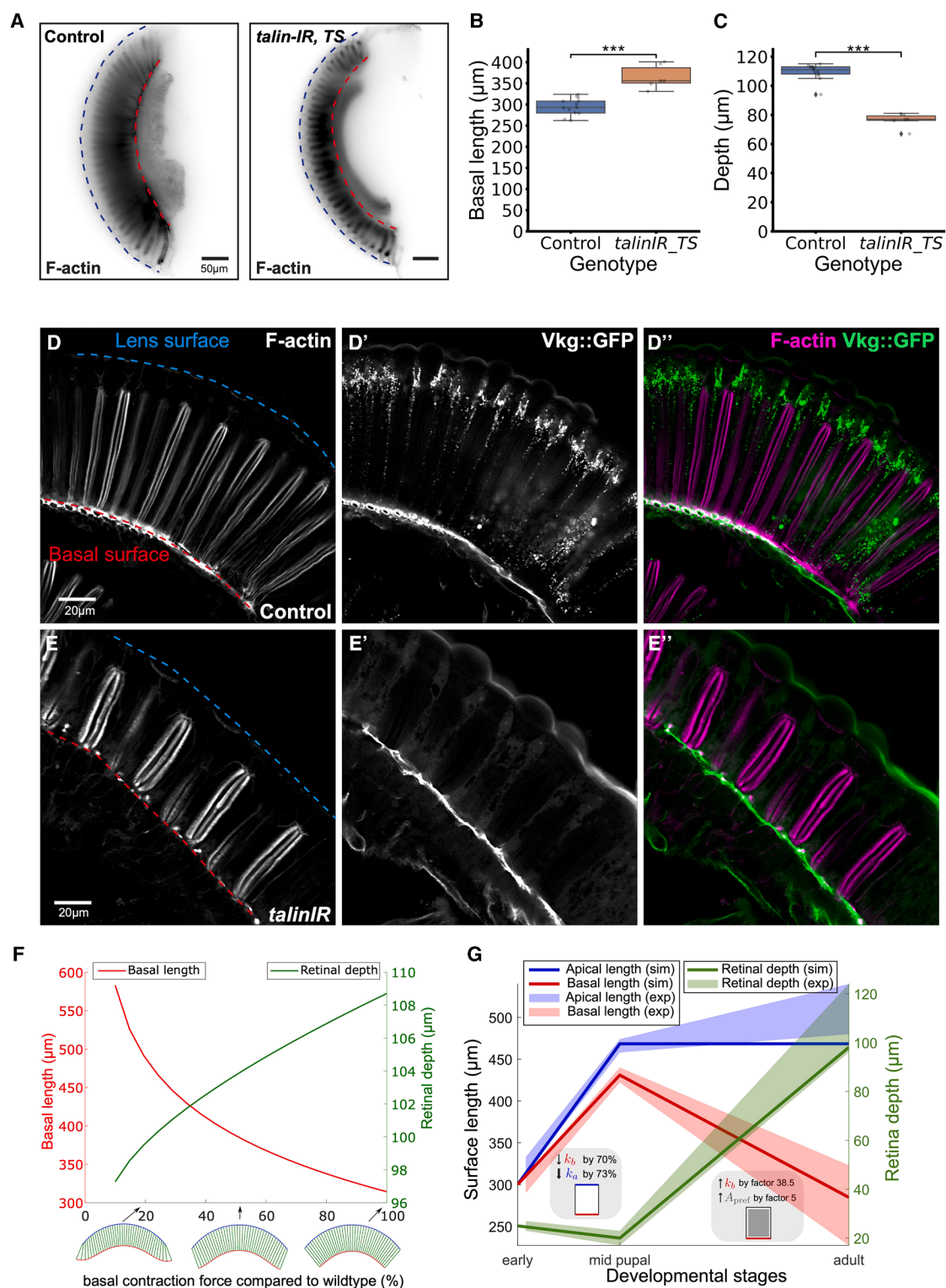


Figure 7. Integrins are required for retinal tissue thickening

(A) Optical sections from light sheet microscopy of retinas expressing GMR-Gal4, Gal80ts, and *talinRNAi*, which were temperature-shifted at 42 h APF to allow temporal control over *talinRNAi* at the onset of basal contraction. Scale bar, 50 μm.

(B) Quantification of basal surface length in *talinRNAi* retinas compared with wild-type control retinas. $n = 6$ retinas and $n = 11$ retinas for *talinRNAi* and wild type, respectively.

(legend continued on next page)

Current Biology

Article



consistent with our previous finding that apical-medial meshworks of MyoII are essential in retinal cell morphogenesis by controlling the apical area of these cells; inhibiting MyoII leads to retinal cell apical area expansion.¹⁴ Examining MyoII function at the basal surface confirms a previous report that it is required for basal contraction.⁴⁴ Moreover, our results show that MyoII is required for cell elongation and, therefore, tissue thickening. Although it is possible that MyoII regulated cell lateral elongation, for example, by modulating cell lateral tension, we note that our computational model does not need such lateral tension regulation for generating the adult eye shape.

When we explored which cell types might promote retinal tissue thickening, we found that photoreceptor elongation is dispensable. This finding differs from a recent report exploring the role of Abl-kinase in retinal development and suggesting a link between photoreceptor morphogenesis and retinal tissue thickening.⁶⁷ The *crb* loss-of-function manipulation we used here specifically affects photoreceptor elongation; this gene is not required for the morphogenesis of any other retinal cell type. Therefore, we propose that cell basal contraction and elongation is coordinated in the IOCs to promote tissue thickening.

Combining our simulations of retinal curvature and tissue thickening allows for simulating pupal retinal development with remarkable accuracy (Figure 7G), suggesting that adhesion, tension, and growth are the main parameters that underpin this process. Many epithelia form tubes with varying degrees of curvature. Based on our work and a previous study in the zebrafish retina,⁶⁶ we anticipate that any instances of curved tissue thickening will require either a reduction in lateral tension or an increase in basal tension. The two scenarios, predicted by our computational model, may reflect different evolutionary solutions to the isotropic growth of a curved epithelium. The specific mechanism underlying tissue thickening may depend on the cell type involved or parameters extrinsic to the tissue. In the fly retina, integrin regulation appears key for the coordination of cell basal contraction and elongation. It will be interesting to determine how these two processes are linked downstream of integrin.

RESOURCE AVAILABILITY

Lead contact

Further information and requests for resources and reagents should be directed to, and will be fulfilled by, the lead contact, Franck Pichaud (f.pichaud@ucl.ac.uk).

(C) Quantification of retinal depth in *talinRNAi* retinas compared with wild-type control retinas. $n = 6$ retinas and $n = 13$ retinas for *talinRNAi* and wild type, respectively. t test. * $p \leq 0.05$, ** $p \leq 0.01$, *** $p \leq 0.001$.

(D) Confocal sagittal section of a control retina at 72 h APF stained with phalloidin to label F-actin. Blue dotted line represents the apical lens surface, and the red dotted line represents the retinal basal surface. Scale bar, 20 μm .

(D') Viking::GFP.

(D'') Merged images with F-actin in magenta and Vkg::GFP in green.

(E) Confocal sagittal section of a retina at 72 h APF stained with phalloidin to label F-actin. The retina expresses GMR-Gal4 and UAS-*talinRNAi*. Blue dotted line represents the apical lens surface, and the red dotted line represents the retinal basal surface. Scale bar, 20 μm .

(E') Viking::GFP.

(E'') Merged images with F-actin in magenta and Vkg::GFP in green.

(F) Simulated basal length (left y axis) and simulated retinal depth (right y axis) at equilibrium if the basal tension is reduced as compared with wild-type adult parameter values. Snapshots below show equilibrium shapes at different basal tension values. Blue represents the apical surface, red represents the basal surface, and green represents the lateral surface of simulated retinas. For details on parameter values and computational methods, see Methods S1.

(G) Simulated apical and basal length (left y axis) and retinal depth (right y axis) for determined best parameter values at early development (0 h), the mid-pupal stage (50 h), and the adult stage. For details on parameter values and computational methods, see Methods S1.

See also Figures S7–S9.

Materials availability

All fly lines made or used in the study are available upon request.

Data and code availability

- All data reported in this article will be shared by the [lead contact](#) upon request. The vertex model code is available: https://github.com/angelikamanhart/Code_Ommatidia_Sheet.
- Any additional information required to reanalyze the data reported in this article is available from the [lead contact](#) upon request.

ACKNOWLEDGMENTS

We would like to thank A. Vaughan, K. Hng, C. Thrasivoulou, M. Redd, A. Grieg, and V. Silio for their training and assistance to C.L. with Airyscan confocal and light sheet imaging. We also thank all Pichaud lab members for their valuable input and comments throughout this work. Work in the Pichaud lab is funded by grants from the MRC (MC_UU_12018/3), the BBSRC (BB/R000697), Wellcome (218278/Z/19/Z), and the Royal Society (award number 181274). C.L. is funded through the UCL Wellcome Optical Biology PhD program (218530/Z/19/Z).

AUTHOR CONTRIBUTIONS

F.P. conceived the project together with C.L. and supervised the work. A.M. designed and developed the computational model with the assistance of C. L. C.L. designed, performed, and analyzed the experiments. F.P., C.L., and A.M. all contributed to writing the manuscript and preparing the figures.

DECLARATION OF INTERESTS

The authors declare no competing interests.

STAR METHODS

Detailed methods are provided in the online version of this paper and include the following:

- [KEY RESOURCES TABLE](#)
- [EXPERIMENTAL MODEL AND STUDY PARTICIPANT DETAILS](#)
- [METHOD DETAILS](#)
 - Fixation and phalloidin staining
 - Confocal image acquisition
 - Light sheet microscopy mounting and imaging
 - Laser ablation
 - Quantifications of tissue and cell metrics
- [QUANTIFICATION AND STATISTICAL ANALYSIS](#)

SUPPLEMENTAL INFORMATION

Supplemental information can be found online at <https://doi.org/10.1016/j.cub.2025.05.048>.

Received: January 4, 2024

Revised: April 11, 2025

Accepted: May 21, 2025

REFERENCES

- Gómez-Gálvez, P., Vicente-Munuera, P., Tagua, A., Forja, C., Castro, A.M., Letrán, M., Valencia-Expósito, A., Grima, C., Bermúdez-Gallardo, M., Serrano-Pérez-Higueras, Ó., et al. (2018). Scutoids are a geometrical solution to three-dimensional packing of epithelia. *Nat. Commun.* 9, 2960. <https://doi.org/10.1038/s41467-018-05376-1>.
- Lou, Y., Rupprecht, J.-F., Theis, S., Hiraiwa, T., and Saunders, T.E. (2023). Curvature-induced cell rearrangements in biological tissues. *Phys. Rev. Lett.* 130, 108401. <https://doi.org/10.1103/PhysRevLett.130.108401>.
- Sui, L., Alt, S., Weigert, M., Dye, N., Eaton, S., Jug, F., Myers, E.W., Jülicher, F., Salbreux, G., and Dahmann, C. (2018). Differential lateral and basal tension drive folding of *Drosophila* wing discs through two distinct mechanisms. *Nat. Commun.* 9, 4620. <https://doi.org/10.1038/s41467-018-06497-3>.
- Sun, Z., Amourda, C., Shagirov, M., Hara, Y., Saunders, T.E., and Toyama, Y. (2017). Basolateral protrusion and apical contraction cooperatively drive *Drosophila* germ-band extension. *Nat. Cell Biol.* 19, 375–383. <https://doi.org/10.1038/ncb3497>.
- Collinet, C., and Lecuit, T. (2021). Programmed and self-organized flow of information during morphogenesis. *Nat. Rev. Mol. Cell Biol.* 22, 245–265. <https://doi.org/10.1038/s41580-020-00318-6>.
- Harris, T.J.C. (2012). Adherens junction assembly and function in the *Drosophila* embryo. *Int. Rev. Cell Mol. Biol.* 293, 45–83. <https://doi.org/10.1016/B978-0-12-394304-0.00007-5>.
- Heisenberg, C.-P., and Bellaïche, Y. (2013). Forces in tissue morphogenesis and patterning. *Cell* 153, 948–962. <https://doi.org/10.1016/j.cell.2013.05.008>.
- Bertet, C., Sulak, L., and Lecuit, T. (2004). Myosin-dependent junction remodelling controls planar cell intercalation and axis elongation. *Nature* 429, 667–671. <https://doi.org/10.1038/nature02590>.
- Rauzi, M., Lenne, P.-F., and Lecuit, T. (2010). Planar polarized actomyosin contractile flows control epithelial junction remodelling. *Nature* 468, 1110–1114. <https://doi.org/10.1038/nature09566>.
- Tetley, R.J., Blanchard, G.B., Fletcher, A.G., Adams, R.J., and Sanson, B. (2016). Unipolar distributions of junctional Myosin II identify cell stripe boundaries that drive cell intercalation throughout *Drosophila* axis extension. *eLife* 5, e12094. <https://doi.org/10.7554/eLife.12094>.
- Zallen, J.A., and Wieschaus, E. (2004). Patterned gene expression directs bipolar planar polarity in *Drosophila*. *Dev. Cell* 6, 343–355. [https://doi.org/10.1016/S1534-5807\(04\)00060-7](https://doi.org/10.1016/S1534-5807(04)00060-7).
- Curran, S., Strandkvist, C., Bathmann, J., De Gennes, M., Kabla, A., Salbreux, G., and Baum, B. (2017). Myosin II controls junction fluctuations to guide epithelial tissue ordering. *Dev. Cell* 43, 480–492.e6. <https://doi.org/10.1016/j.devcel.2017.09.018>.
- Bao, S., and Cagan, R. (2005). Preferential adhesion mediated by Hibris and Roughest regulates morphogenesis and patterning in the *Drosophila* eye. *Dev. Cell* 8, 925–935. <https://doi.org/10.1016/j.devcel.2005.03.011>.
- Blackie, L., Walther, R.F., Staddon, M.F., Banerjee, S., and Pichaud, F. (2020). Cell-type-specific mechanical response and myosin dynamics during retinal lens development in *Drosophila*. *Mol. Biol. Cell* 31, 1355–1369. <https://doi.org/10.1091/mbc.E19-09-0523>.
- Blackie, L., Tozluoglu, M., Trylinski, M., Walther, R.F., Schweiguth, F., Mao, Y., and Pichaud, F. (2021). A combination of Notch signaling, preferential adhesion and endocytosis induces a slow mode of cell intercalation in the *Drosophila* retina. *Development* 148, dev197301. <https://doi.org/10.1242/dev.197301>.
- Malin, J., Rosa Birriel, C., Astigarraga, S., Treisman, J.E., and Hatini, V. (2022). Sidekick dynamically rebalances contractile and protrusive forces to control tissue morphogenesis. *J. Cell Biol.* 221, e202107035. <https://doi.org/10.1083/jcb.202107035>.
- Pichaud, F. (2014). Transcriptional regulation of tissue organization and cell morphogenesis: The fly retina as a case study. *Dev. Biol.* 385, 168–178. <https://doi.org/10.1016/j.ydbio.2013.09.031>.
- Pinheiro, D., and Bellaïche, Y. (2018). Mechanical force-driven adherens junction remodeling and epithelial dynamics. *Dev. Cell* 47, 3–19. <https://doi.org/10.1016/j.devcel.2018.09.014>.
- Takeichi, M. (2014). Dynamic contacts: rearranging adherens junctions to drive epithelial remodelling. *Nat. Rev. Mol. Cell Biol.* 15, 397–410. <https://doi.org/10.1038/nrm3802>.
- Corrigall, D., Walther, R.F., Rodriguez, L., Fichelson, P., and Pichaud, F. (2007). Hedgehog signaling is a principal inducer of myosin-II-driven cell ingress in *Drosophila* epithelia. *Dev. Cell* 13, 730–742. <https://doi.org/10.1016/j.devcel.2007.09.015>.
- Martin, A.C., Kaschube, M., and Wieschaus, E.F. (2009). Pulsed contractions of an actin–myosin network drive apical constriction. *Nature* 457, 495–499. <https://doi.org/10.1038/nature07522>.
- Martin, A.C., and Goldstein, B. (2014). Apical constriction: themes and variations on a cellular mechanism driving morphogenesis. *Development* 141, 1987–1998. <https://doi.org/10.1242/dev.102228>.
- Rauzi, M., Krzic, U., Saunders, T.E., Krajnc, M., Ziherl, P., Hufnagel, L., and Leptin, M. (2015). Embryo-scale tissue mechanics during *Drosophila* gastrulation movements. *Nat. Commun.* 6, 8677. <https://doi.org/10.1038/ncomms9677>.
- López-Gay, J.M., Nunley, H., Spencer, M., Di Pietro, F., Guirao, B., Bosveld, F., Markova, O., Gaugue, I., Pelletier, S., Lubensky, D.K., et al. (2020). Apical stress fibers enable a scaling between cell mechanical response and area in epithelial tissue. *Science* 370, eabb2169. <https://doi.org/10.1126/science.abb2169>.
- Khalilgharibi, N., and Mao, Y. (2021). To form and function: on the role of basement membrane mechanics in tissue development, homeostasis and disease. *Open Biol.* 11, 200360. <https://doi.org/10.1098/rsob.200360>.
- Kular, J.K., Basu, S., and Sharma, R.I. (2014). The extracellular matrix: Structure, composition, age-related differences, tools for analysis and applications for tissue engineering. *J. Tissue Eng.* 5, 2041731414557112. <https://doi.org/10.1177/2041731414557112>.
- Cerqueira Campos, F., Dennis, C., Alégot, H., Fritsch, C., Isabella, A., Pouchin, P., Bardot, O., Horne-Badovinac, S., and Mirouse, V. (2020). Oriented basement membrane fibrils provide a memory for F-actin planar polarization via the Dystrophin-Dystroglycan complex during tissue elongation. *Development* 147, dev186957. <https://doi.org/10.1242/dev.186957>.
- Crest, J., Díz-Muñoz, A., Chen, D.-Y., Fletcher, D.A., and Bilder, D. (2017). Organ sculpting by patterned extracellular matrix stiffness. *eLife* 6, e24958. <https://doi.org/10.7554/eLife.24958>.
- Díaz-de-la-Loza, M.-D.-C., and Stramer, B.M. (2024). The extracellular matrix in tissue morphogenesis: No longer a backseat driver. *Cells Dev.* 177, 203883. <https://doi.org/10.1016/j.cdev.2023.203883>.
- Horne-Badovinac, S. (2020). Mobilizing the matrix for organ morphogenesis. *Dev. Cell* 54, 1–2. <https://doi.org/10.1016/j.devcel.2020.06.014>.
- Ramos-Lewis, W., and Page-McCaw, A. (2019). Basement membrane mechanics shape development: Lessons from the fly. *Matrix Biol.* 75–76, 72–81. <https://doi.org/10.1016/j.matbio.2018.04.004>.
- Santa-Cruz Mateos, C., Valencia-Expósito, A., Palacios, I.M., and Martín-Bermudo, M.D. (2020). Integrins regulate epithelial cell shape by controlling the architecture and mechanical properties of basal actomyosin networks. *PLoS Genet.* 16, e1008717. <https://doi.org/10.1371/journal.pgen.1008717>.

Current Biology

Article



33. Nematbakhsh, A., Levis, M., Kumar, N., Chen, W., Zartman, J.J., and Alber, M. (2020). Epithelial organ shape is generated by patterned actomyosin contractility and maintained by the extracellular matrix. *PLoS Comput. Biol.* 16, e1008105. <https://doi.org/10.1371/journal.pcbi.1008105>.
34. Nicolás-Pérez, M., Kuchling, F., Letelier, J., Polvillo, R., Wittbrodt, J., and Martínez-Morales, J.R. (2016). Analysis of cellular behavior and cytoskeletal dynamics reveal a constriction mechanism driving optic cup morphogenesis. *eLife* 5, e15797. <https://doi.org/10.7554/eLife.15797>.
35. Gutzman, J.H., Graeden, E., Brachmann, I., Yamazoe, S., Chen, J.K., and Sive, H. (2018). Basal constriction during midbrain-hindbrain boundary morphogenesis is mediated by Wnt5b and focal adhesion kinase. *Biol. Open* 7, bio034520. <https://doi.org/10.1242/bio.034520>.
36. Gutzman, J.H., Graeden, E.G., Lowery, L.A., Holley, H.S., and Sive, H. (2008). Formation of the zebrafish midbrain-hindbrain boundary constriction requires laminin-dependent basal constriction. *Mech. Dev.* 125, 974–983. <https://doi.org/10.1016/j.mod.2008.07.004>.
37. Bachmann, M., Kukkainen, S., Hytönen, V.P., and Wehrle-Haller, B. (2019). Cell adhesion by integrins. *Physiol. Rev.* 99, 1655–1699. <https://doi.org/10.1152/physrev.00036.2018>.
38. Bunch, T.A., and Brower, D.L. (1992). Drosophila PS2 integrin mediates RGD-dependent cell-matrix interactions. *Development* 116, 239–247. <https://doi.org/10.1242/dev.116.1.239>.
39. Kechagia, J.Z., Ivaska, J., and Roca-Cusachs, P. (2019). Integrins as biomechanical sensors of the microenvironment. *Nat. Rev. Mol. Cell Biol.* 20, 457–473. <https://doi.org/10.1038/s41580-019-0134-2>.
40. Bogdanović, O., Delfino-Machín, M., Nicolás-Pérez, M., Gavilán, M.P., Gago-Rodrigues, I., Fernández-Miñán, A., Lillo, C., Ríos, R.M., Wittbrodt, J., and Martínez-Morales, J.R. (2012). Numb/Numbl-Opo antagonism controls retinal epithelium morphogenesis by regulating integrin endocytosis. *Dev. Cell* 23, 782–795. <https://doi.org/10.1016/j.devcel.2012.09.004>.
41. Martinez-Morales, J.R., Rembold, M., Greger, K., Simpson, J.C., Brown, K.E., Quiring, R., Pepperkok, R., Martin-Bermudo, M.D., Himmelbauer, H., and Wittbrodt, J. (2009). ojoplano-mediated basal constriction is essential for optic cup morphogenesis. *Development* 136, 2165–2175. <https://doi.org/10.1242/dev.033563>.
42. Casey, M.A., Lusk, S., and Kwan, K.M. (2021). Build me up optic cup: Intrinsic and extrinsic mechanisms of vertebrate eye morphogenesis. *Dev. Biol.* 476, 128–136. <https://doi.org/10.1016/j.ydbio.2021.03.023>.
43. Walther, R.F., Lancaster, C., Burden, J.J., and Pichaud, F. (2024). A dystroglycan-laminin-integrin axis coordinates cell shape remodeling in the developing Drosophila retina. *PLoS Biol.* 22, e3002783. <https://doi.org/10.1371/journal.pbio.3002783>.
44. Ready, D.F., and Chang, H.C. (2021). Calcium waves facilitate and coordinate the contraction of endfeet actin stress fibers in *Drosophila* interommatidial cells. *Development* 148, dev199700. <https://doi.org/10.1242/dev.199700>.
45. Cagan, R.L., and Ready, D.F. (1989). The emergence of order in the *Drosophila* pupal retina. *Dev. Biol.* 136, 346–362. [https://doi.org/10.1016/0012-1606\(89\)90261-3](https://doi.org/10.1016/0012-1606(89)90261-3).
46. Longley, R.L., and Ready, D.F. (1995). Integrins and the development of three-dimensional structure in the *Drosophila* compound eye. *Dev. Biol.* 171, 415–433. <https://doi.org/10.1006/dbio.1995.1292>.
47. Cagan, R. (2009). Principles of *Drosophila* eye differentiation. *Curr. Top. Dev. Biol.* 89, 115–135. [https://doi.org/10.1016/S0070-2153\(09\)89005-4](https://doi.org/10.1016/S0070-2153(09)89005-4).
48. Ready, D.F., Hanson, T.E., and Benzer, S. (1976). Development of the *Drosophila* retina, a neurocrystalline lattice. *Dev. Biol.* 53, 217–240. [https://doi.org/10.1016/0012-1606\(76\)90225-6](https://doi.org/10.1016/0012-1606(76)90225-6).
49. Walther, R.F., and Pichaud, F. (2010). Crumbs/DaPKC-dependent apical exclusion of Bazooka promotes photoreceptor polarity remodeling. *Curr. Biol.* 20, 1065–1074. <https://doi.org/10.1016/j.cub.2010.04.049>.
50. Pichaud, F., and Casares, F. (2022). Shaping an optical dome: The size and shape of the insect compound eye. *Semin. Cell Dev. Biol.* 130, 37–44. <https://doi.org/10.1016/j.semcdcb.2021.11.002>.
51. Charlton-Perkins, M., Brown, N.L., and Cook, T.A. (2011). The lens in focus: a comparison of lens development in *Drosophila* and vertebrates. *Mol. Genet. Genomics* 286, 189–213. <https://doi.org/10.1007/s00438-011-0643-y>.
52. Farhadifar, R., Röper, J.-C., Aigouy, B., Eaton, S., and Jülicher, F. (2007). The influence of cell mechanics, cell-cell interactions, and proliferation on epithelial packing. *Curr. Biol.* 17, 2095–2104. <https://doi.org/10.1016/j.cub.2007.11.049>.
53. Misra, M., Audoly, B., Kevrekidis, I.G., and Shvartsman, S.Y. (2016). Shape transformations of epithelial shells. *Biophys. J.* 110, 1670–1678. <https://doi.org/10.1016/j.bpj.2016.03.009>.
54. Štorgel, N., Krajnc, M., Mrak, P., Štrus, J., and Ziherl, P. (2016). Quantitative morphology of epithelial folds. *Biophys. J.* 110, 269–277. <https://doi.org/10.1016/j.bpj.2015.11.024>.
55. Stahl, A.L., Charlton-Perkins, M., Buschbeck, E.K., and Cook, T.A. (2017). The cuticular nature of corneal lenses in *Drosophila melanogaster*. *Dev. Genes Evol.* 227, 271–278. <https://doi.org/10.1007/s00427-017-0582-7>.
56. Goberdhan, D.C.I., Paricio, N., Goodman, E.C., Mlodzik, M., and Wilson, C. (1999). *Drosophila* tumor suppressor PTEN controls cell size and number by antagonizing the Chico/PI3-kinase signaling pathway. *Genes Dev.* 13, 3244–3258. <https://doi.org/10.1101/gad.13.24.3244>.
57. Izaddoost, S., Nam, S.-C., Bhat, M.A., Bellen, H.J., and Choi, K.-W. (2002). *Drosophila* Crumbs is a positional cue in photoreceptor adherens junctions and rhabdomeres. *Nature* 416, 178–183. <https://doi.org/10.1038/nature720>.
58. Pellikka, M., Tanentzapf, G., Pinto, M., Smith, C., McGlade, C.J., Ready, D.F., and Tepass, U. (2002). Crumbs, the *Drosophila* homologue of human CRB1/RP12, is essential for photoreceptor morphogenesis. *Nature* 416, 143–149. <https://doi.org/10.1038/nature721>.
59. Tepaß, U., and Knust, E. (1990). Phenotypic and developmental analysis of mutations at thecrumbs locus, a gene required for the development of epithelia in *Drosophila melanogaster*. *Roux's Arch. Dev. Biol.* 199, 189–206. <https://doi.org/10.1007/BF01682078>.
60. Richardson, E.C.N., and Pichaud, F. (2010). Crumbs is required to achieve proper organ size control during *Drosophila* head development. *Development* 137, 641–650. <https://doi.org/10.1242/dev.041913>.
61. Dawes-Hoang, R.E., Parmar, K.M., Christiansen, A.E., Phelps, C.B., Brand, A.H., and Wieschaus, E.F. (2005). *folded gastrulation*, cell shape change and the control of myosin localization. *Development* 132, 4165–4178. <https://doi.org/10.1242/dev.01938>.
62. Martin-Bermudo, M.D., and Brown, N.H. (1999). Uncoupling integrin adhesion and signaling: the betaPS cytoplasmic domain is sufficient to regulate gene expression in the *Drosophila* embryo. *Genes Dev.* 13, 729–739. <https://doi.org/10.1101/gad.13.6.729>.
63. Klapholz, B., and Brown, N.H. (2017). Talin – the master of integrin adhesions. *J. Cell Sci.* 130, 2435–2446. <https://doi.org/10.1242/jcs.190991>.
64. McGuire, S.E., Le, P.T., Osborn, A.J., Matsumoto, K., and Davis, R.L. (2003). Spatiotemporal rescue of memory dysfunction in *Drosophila*. *Science* 302, 1765–1768. <https://doi.org/10.1126/science.1089035>.
65. Morin, X., Daneman, R., Zavortink, M., and Chia, W. (2001). A protein trap strategy to detect GFP-tagged proteins expressed from their endogenous loci in *Drosophila*. *Proc. Natl. Acad. Sci. USA* 98, 15050–15055. <https://doi.org/10.1073/pnas.261408198>.
66. Matejčić, M., Salbreux, G., and Norden, C. (2018). A non-cell-autonomous actin redistribution enables isotropic retinal growth. *PLoS Biol.* 16, e2006018. <https://doi.org/10.1371/journal.pbio.2006018>.
67. Sun, X., Decker, J., Sanchez-Luege, N., and Rebay, I. (2024). Inter-plane feedback coordinates cell morphogenesis and maintains 3D tissue organization in the *Drosophila* pupal retina. *Development* 151, dev201757. <https://doi.org/10.1242/dev.201757>.

68. Freeman, M. (1996). Reiterative use of the EGF receptor triggers differentiation of all cell types in the *Drosophila* eye. *Cell* 87, 651–660. [https://doi.org/10.1016/S0092-8674\(00\)81385-9](https://doi.org/10.1016/S0092-8674(00)81385-9).
69. Chan, E.H., ChavadiShivakumar, P., Clément, R., Laugier, E., and Lenne, P.-F. (2017). Patterned cortical tension mediated by N-cadherin controls cell geometric order in the *Drosophila* eye. *eLife* 6, e22796. <https://doi.org/10.7554/eLife.22796>.
70. Royou, A., Field, C., Sisson, J.C., Sullivan, W., and Karess, R. (2004). Reassessing the role and dynamics of nonmuscle myosin II during furrow formation in early *Drosophila* embryos. *Mol. Biol. Cell* 15, 838–850. <https://doi.org/10.1091/mbc.e03-06-0440>.
71. Bosch, J.A., Tran, N.H., and Hariharan, I.K. (2015). CoinFLP: a system for efficient mosaic screening and for visualizing clonal boundaries in *Drosophila*. *Development* 142, 597–606. <https://doi.org/10.1242/dev.114603>.
72. Schindelin, J., Arganda-Carreras, I., Frise, E., Kaynig, V., Longair, M., Pietzsch, T., Preibisch, S., Rueden, C., Saalfeld, S., Schmid, B., et al. (2012). Fiji: an open-source platform for biological-image analysis. *Nat. Methods* 9, 676–682. <https://doi.org/10.1038/nmeth.2019>.
73. Meijering, E., Dzyubachyk, O., and Smal, I. (2012). Methods for cell and particle tracking. *Methods Enzymol.* 504, 183–200. <https://doi.org/10.1016/B978-0-12-391857-4.00009-4>.
74. Mary, H., and Brouhard, G.J. (2019). Kappa (κ): analysis of curvature in biological image data using B-splines. Preprint at bioRxiv. <https://doi.org/10.1101/852772>.
75. Hunter, J.D. (2007). Matplotlib: a 2D graphics environment. *Comput. Sci. Eng.* 9, 90–95. <https://doi.org/10.1109/MCSE.2007.55>.
76. Waskom, M. (2021). seaborn: statistical data visualization. *JOSS* 6, 3021. <https://doi.org/10.21105/joss.03021>.
77. Virtanen, P., Gommers, R., Oliphant, T.E., Haberland, M., Reddy, T., Cournapeau, D., Burovski, E., Peterson, P., Weckesser, W., Bright, J., et al. (2020). SciPy 1.0: fundamental algorithms for scientific computing in Python. *Nat. Methods* 17, 261–272. <https://doi.org/10.1038/s41592-019-0686-2>.
78. McKinney, W. (2010). Data structures for statistical computing in Python. *Proceedings of the Python in Science Conference*, 56–61. <https://doi.org/10.25080/Majora-92bf1922-00a>.
79. Walther, R.F., and Pichaud, F. (2006). Immunofluorescent staining and imaging of the pupal and adult *Drosophila* visual system. *Nat. Protoc.* 1, 2635–2642. <https://doi.org/10.1038/nprot.2006.379>.

STAR★METHODS

KEY RESOURCES TABLE

REAGENT or RESOURCE	SOURCE	IDENTIFIER
Antibodies		
Mouse monoclonal anti betaPS (Myospheroid)	Developmental Studies Hybridoma Bank	Cat#CF.6G11
Anti-CF 405S Goat Anti-Mouse IgG	Biotium	Cat#20830
Chemicals, peptides, and recombinant proteins		
Triton-x-100	Sigma-Aldrich	Cat#T8787
Low melting point agarose	Sigma-Aldrich	Cat#A4018
Formaldehyde	Sigma-Aldrich	Cat#F8775
Shields and Sang M3 media	Sigma-Aldrich	Cat#S3652
Fetal Bovine Serum	Sigma-Aldrich	Cat#F0926
Hydroxyecdysone	Sigma-Aldrich	Cat#H5142
Insulin	Sigma-Aldrich	Cat#I0516
Penicillin-Streptomycin	Thermo Fisher Scientific	Cat#15140-122
Vectashield Antifade mounting medium	Vector Laboratories	Cat#H-1000-10
Phalloidin Atto 565	Sigma-Aldrich	Cat#94072
Deposited data		
Vertex model	This paper	https://github.com/angelikamanhart/Code_Ommatidia_Sheet
Experimental models: Organisms/strains		
<i>D. melanogaster</i> , <i>yw</i> ;;;	Pichaud lab stock	N/A
<i>D. melanogaster</i> ,;GMR-Gal4;	Freeman ⁶⁸	N/A
<i>D. melanogaster</i> , <i>Ecad:GFP</i> ; <i>myrRFP</i>	Chan et al. ⁶⁹	N/A
<i>D. melanogaster</i> , <i>y,w</i> , <i>sqhAX3</i> ; <i>sqh>sqhGFP</i> ;	Rouyou et al. ⁷⁰ ; Bloomington Drosophila Stock Center	BDSC 57144
<i>D. melanogaster</i> ,;UAS-YFP-myosinII (Zip)-Dominant-Negative;	Dawes-Hoang et al. ⁶¹	N/A
<i>D. melanogaster</i> ,;UAS-Torso::Mys ^{DN} ;	Martin-Bermudo and Brown ⁶²	N/A
<i>D. melanogaster</i> ,;UAS-Talin RNAi	Vienna Drosophila Resource Center	VDRC 40339
<i>D. melanogaster</i> ,;sqh::Utrophin::GFP	Rauzi et al. ⁹	N/A
<i>D. melanogaster</i> ,;CoinFLP-Gal4 attP40;	Bosch et al. ⁷¹ ; Bloomington Drosophila Stock Center	BDSC 59270
<i>D. melanogaster</i> , <i>w</i> ; GMR-Gal4; tubP-Gal80ts	McGuire et al. ⁶⁴ ; Bloomington Drosophila Stock Center	BDSC 7017
<i>D. melanogaster</i> ,;Vkg::GFP; GMR-Gal4	This study; Vkg::GFP from Bloomington Drosophila Stock Center; Morin et al. ⁶⁵	BDSC 98343
<i>D. melanogaster</i> , <i>w</i> ; PTEN ³ , FRT40A/Cyo	Goberdhan et al. ⁵⁶	Gift from Clive Wilson
<i>D. melanogaster</i> , <i>w</i> ; PTEN ¹ , FRT40A/Cyo	Goberdhan et al. ⁵⁶	Gift from Clive Wilson
<i>D. melanogaster</i> , <i>y,w</i> ; GMRhid-cl, FRT40A/Cyo; ey-FLP, UAS-FLP, GMR-hid (EGUF)	Bloomington Drosophila Stock Center	BDSC 76594
Software and algorithms		
FIJI	Schindelin et al. ⁷²	https://imagej.net/software/fiji/
ImageJ, MtrackJ	Meijering et al. ⁷³	https://imagej.net/plugins/mtrackj
ImageJ, Kappa curvature analysis	Mary and Brouhard ⁷⁴	https://imagej.net/plugins/kappa
Imaris 9.1.2	Oxford Instruments	https://imaris.oxinst.com
Matlab	MathWorks	https://www.mathworks.com/products/matlab.htmmys
Python v3.9.19	Python Software Foundation	https://www.python.org

(Continued on next page)

Continued

REAGENT or RESOURCE	SOURCE	IDENTIFIER
Matplotlib v3.5.2	Hunter ⁷⁵	https://github.com/matplotlib/matplotlib
Seaborn v0.11.2	Waskom ⁷⁶	https://github.com/mwaskom/seaborn
Scipy v1.7.3	Virtanen et al. ⁷⁷	https://github.com/scipy/scipy
Pandas v1.4.3	McKinney ⁷⁸	https://github.com/pandas-dev/pandas
Adobe Illustrator 29.2.1	Adobe	https://www.adobe.com
Adobe Photoshop	Adobe	https://www.adobe.com
Inkscape	N/A	https://inkscape.org
Other		
Transparent double-sided tape (Tesa)	Rapid Electronics	Cat#05338

EXPERIMENTAL MODEL AND STUDY PARTICIPANT DETAILS

Flies were raised on standard food at 18 °C. Crosses were performed at 25°C unless stated otherwise. For strain details please consult the [key resources table](#).

METHOD DETAILS

Fixation and phalloidin staining

Pupae were stored and staged at 18°C and 25°C and allowed to develop to the appropriate stage.⁷⁹ Retinas were dissected in PBS on ice and fixed in 4% paraformaldehyde solution for 25 minutes at room temperature. Adult retinas were fixed in 4% paraformaldehyde for at least 35 minutes. Retinas were then washed 3 times in PBS-T. If primary antibodies were used, they were added in PBS-T overnight at 4°C. Retinas were then washed 3 times in PBS-T and then incubated with phalloidin in PBS-T overnight at 4°C. Retinas were then washed in PBS-T for at least 4 hours (adults were washed overnight). Retinas were mounted on glass slides with Vectashield (Vectorlabs). Phalloidin was used at 1:200 (phalloidin565 (Sigma), to visualize F-actin.

Confocal image acquisition

Images of fixed retinas were acquired on a Zeiss LSM900 in confocal mode or with an Airyscan detector for higher resolution and signal to noise ratio. Retinas were imaged with a 63x oil objective lens.

Light sheet microscopy mounting and imaging

Live pupae or fixed retinas were mounted in 2% low melting point agarose.

To mount animals or retina, 1-2mL of molten agarose was decanted onto parafilm and samples were pipetted into the agarose under a dissecting microscope. Using a capillary tube (Zeiss), samples were sucked into the capillary and left to solidify for 3-4 minutes before being placed into the imaging chamber. The imaging chamber was filled with distilled water. 10x and 5x water immersion objective lenses were used for light sheet acquisition and illumination respectively. Samples were imaged on a Zeiss Light sheet Z.1 microscope.

Laser ablation

To perform laser ablations, retinas were dissected out of appropriately staged pupae (42h APF and 65h APF) in Shields and Sang M3 media supplemented with 2% FBS, 1% pen/strep, 3ng/ml ecdysone, and 2ng/ml insulin. Retinas were mounted between two coverslips separated by extra thin double-sided tape. Retinas were imaged on a Zeiss LSM880 upright microscope with a 63x oil objective lens. Laser ablations were performed using a pulsed Chameleon Ti Sapphire laser tuned to 760nm. Ablations were performed on manually defined rectangular ROIs in the center of secondary pigment cells. Ablations were imaged simultaneously with the built-in confocal microscope for 118 seconds using the Airyscan detector. Cell edge displacement was calculated by tracking the end of each cell with mTrackJ⁷³ and calculating the distance between each of the two points over time. Initial recoil velocity was calculated from the displacement one frame after the cut.

Quantifications of tissue and cell metrics

Apical, basal, lateral length measurements

Light sheet imaging data were used to measure the apical, basal, and lateral lengths (depth) of the retinas. This was performed using the Fiji segmented line tool to manually draw and measure each surface.

Interommatidial distance

The distance between neighboring ommatidia was measured manually using the line tool in Fiji.

Curvature measurements

Light sheet imaging data was used to measure retinal curvature. This was performed using the image J plug in, Kappa curvature analysis.⁷⁴

3D cell segmentation

3D cell segmentation was performed on samples stained with Ecadherin and phalloidin to segment cell membranes. Airyscan confocal images were processed with default Zeiss Airyscan processing parameters. Images were then processed with Image J using the background subtraction filter (Rolling ball radius 50 pixels) and a gaussian blur filter (Sigma/Radius 1.5) to enhance cell membrane signal for segmentation. Using Imaris 9.1.2, cells were manually segmented. 2D contours were drawn around each cell every two optical sections and surfaces were created to render individual cells in 3D. Volumes were then taken from the surfaces to quantify the data. There were some cases in the 72h APF retinas when segmentation was challenging, and the contours were not drawn every two optical sections. However, in most instances, splines were drawn every two to three optical sections.

Vertex model

See [Methods S1](#).

QUANTIFICATION AND STATISTICAL ANALYSIS

Python was used for statistical analysis and plotting (Matplotlib), apart from modelling results which was plotted in Matlab. For T-tests and Mann-Whitney U tests, the scipy package was used. To test for normality, we performed a Shapiro-Wilk test using the scipy package.